Geometric calibration in X-ray fluorescence computed tomography using opposite-detector consistency conditions

Meo VAN DUIJNEN MONTIJN[1,2] Jérôme LESAINT[1] Jean Michel LÉTANG[2] Simon RIT[2]

[1] ESRF, The European Synchrotron, 71 Avenue des Martyrs, CS40220, 38043 Grenoble Cedex 9, France

[2] INSA-Lyon, Université Claude Bernard Lyon 1, CNRS, Inserm, CREATIS UMR 5220, U1294, F-69373, Lyon, France

Résumé – De nouvelles conditions de cohérence des données (DCC) adaptées à la tomographie par fluorescence X (XFCT) et intégrant explicitement l'auto-absorption sont introduites. Ces DCC permettent d'estimer le centre de rotation à partir d'une seule paire de projections séparées d'un demi-tour et acquises par deux détecteurs opposés. Elles permettent une compensation partielle d'un déplacement rigide de l'échantillon. Cette méthode de calibration est analytique et ne nécessite aucun marqueur.

Abstract – A novel set of data consistency conditions (DCCs) tailored to X-ray fluorescence computed tomography (XFCT) is proposed, explicitly accounting for self-absorption. These DCCs enable estimation of the center of rotation from a single pair of projections separated by half a rotation and acquired from opposing detectors. They also allow for partial compensation of a rigid displacement of the sample. This method offers a marker-free, analytical calibration strategy for XFCT.

1 Introduction

In X-ray fluorescence computed tomography (XFCT), three-dimensional elemental distributions are reconstructed from sets of two-dimensional fluorescence projections. However, reconstruction quality can be compromised by inaccuracies in geometric calibration. This calibration involves the precise determination of the acquisition geometry, and various methods have been developed for X-ray transmission computed tomography (XTCT) setups, ranging from simple parallel-beam configurations to more complex divergent geometries.

In typical XFCT setups, XTCT data can be acquired simultaneously, enabling calibration based on transmission data. However, this approach becomes unreliable when beam attenuation is insufficient, resulting in low contrast in the XTCT data. Consequently, calibration techniques that rely on the XFCT data become necessary.

Marker-based alignment methods prove an effective approach [6], but these require insertion of physical markers into the sample. Alternatively, heuristic methods originally developed for XTCT — such as reprojection-based sample motion correction [2] and autofocus techniques for center-of-rotation estimation [5] — have demonstrated effectiveness in XFCT calibration [1].

Analytical XTCT calibration approaches, particularly those based on the Helgason–Ludwig data consistency conditions (DCCs) [8], have been employed for identifying sample motions [7] and determining the center of rotation [3], but they fail to account for attenuation effects specific to XFCT. To the best of the authors' knowledge, no analytical calibration method exists that is specifically tailored for XFCT.

The major obstacle in developing such methods lies in incorporating attenuation effects, especially since attenuation maps are typically unknown — except at the incoming beam energy when XTCT data is acquired. To address this limitation, a novel set of DCCs tailored to dual-detector XFCT setups is proposed, explicitly incorporating attenuation effects. By correlating fluorescence data acquired from oppositely positioned detectors, this approach facilitates determination of the center of rotation and constrains sample motion.

This paper presents a center-of-rotation determination and motion correction methodology for XFCT based on newly formulated XFCT-specific DCCs. In contrast to traditional transmission-based calibration approaches, this method accounts for attenuation. Validation through simulations demonstrates the effectiveness of this method.

2 Definitions and Notation

2.1 Geometry

Two-dimensional fluorescence projections are acquired by deconvolving off-axis spectral measurements, avoiding detection of the transmitted beam. To localize the fluorescence signal within the sample, collimators may be used [4], though higher spatial resolution is typically achieved with a pencil beam setup. To minimize scattered photon detection, detectors are generally placed at a 90° angle relative to the incident beam. In systems with linearly polarized light, such as those at synchrotron facilities, scatter suppression is further enhanced when detectors lie in the plane of polarization.

In this work, a dual-detector configuration is considered, although the proposed method extends to any number of oppositely placed detector pairs. Two point detectors are positioned far away at 90° on either side of the incident beam, as illustrated in figure 1. Denoting the center of rotation by $\vec{c}$, the clockwise rotation of a point $\vec{q}$ by an angle θ about this center is given by:

$$R_\theta(\vec{q}) = \begin{bmatrix} \cos\theta & \sin\theta \\ -\sin\theta & \cos\theta \end{bmatrix} (\vec{q} - \vec{c}) + \vec{c} \qquad (1)$$

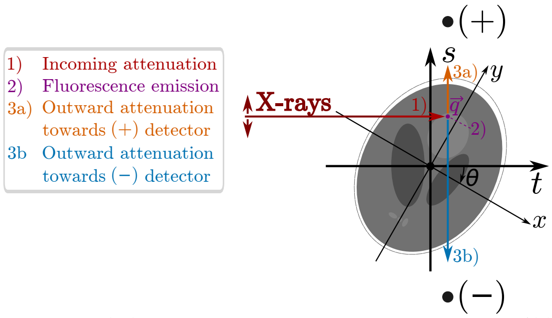

Figure 1 – Dual-detector XFCT system. An X-ray pencil beam propagates in the t-direction and scans the sample along the s-axis, covering all points $\vec{q}$. Two point detectors, $(+)$ and $(-)$, are positioned far from the sample, perpendicular around the beam. The sample rotates clockwise by an angle θ.

2.2 Sample Maps

2.2.1 Fluorescence Map

The intensity of a fluorescence line from an element Z emitted at point $\vec{q}$, denoted by $f_{\text{line}}^{(Z)}(\vec{q}, \theta)$ [cm^{-1}], resulting from an incident beam of energy E_0, is given by:

$$f_{\text{line}}^{(Z)}(\vec{q}, \theta) = \rho^{(Z)}(R_{-\theta}(\vec{q}))\sigma_{\text{line}}^{(Z)}(E_0) \tag{2}$$

where $\rho^{(Z)}(\vec{q})$ [g/cm^3] represents the spatial distribution of element Z, $R_\theta(\vec{q})$ is the rotation matrix defined in equation 1, and $\sigma_{\text{line}}^{(Z)}(E_0)$ [cm^2/g] denotes the effective fluorescence cross-section corresponding to the specified element and emission line at energy E_0. Explicit reference to the element and fluorescence line are omitted hereafter for brevity.

2.2.2 Attenuation and Transmission Maps

The attenuation map $\mu(\vec{q}, E)$ [cm^{-1}] describes how both the incident beam and fluorescence intensities are modulated. It must be known at the excitation energy E_0 and all relevant fluorescence energies. Transmission between any two points follows the Lambert-Beer law, governed by the cumulative attenuation between them. Accordingly, two complementary transmission maps are defined: the first describes the probability of the incident beam reaching a point $\vec{q}$, while the second represents the probability that fluorescence emitted from $\vec{q}$ reaches the $(\pm)$ detector. These are respectively given by:

$$T_{\text{in}}(\vec{q}, \theta) := \exp\left[-\int_0^\infty \mu(R_{-\theta}(\vec{q} - t'\hat{t}), E_0)dt'\right] \tag{3a}$$

$$T_{\text{out}}^{(\pm)}(\vec{q}, \theta) := \exp\left[-\int_0^\infty \mu(R_{-\theta}(\vec{q} \pm s'\hat{s}), E_f)ds'\right] \tag{3b}$$

where $\hat{t}$ and $\hat{s}$ denote unit vectors along the incident and detection directions, respectively. The outward transmission is evaluated at a specified fluorescence energy E_f. Here, the detectors are modeled as point-like and positioned sufficiently far from the sample, such that the cone of detected fluorescence can be approximated by a single ray perpendicular to the incident beam.

2.3 Projection and moment definitions

Given the prior definitions and specified parameters — including the incident energy E_0, element Z, fluorescence line, and corresponding fluorescence energy E_f — and defining the incident beam intensity as I_0, the corresponding fluorescence projections are given by:

$$p^{(\pm)}(s, \theta) = I_0 \int_{-\infty}^{\infty} T_{\text{in}}(\vec{q}, \theta) f(\vec{q}, \theta) T_{\text{out}}^{(\pm)}(\vec{q}, \theta)\Big|_{\vec{q} = s\hat{s} + t\hat{t}} dt \tag{4}$$

interpretable as an attenuation-adjusted 2D Radon transform of $I_0 f(\vec{q}, \theta)$. The model's dependence on $R_\theta(\vec{q})$ again underscores the need for precise center-of-rotation calibration. The n-th order (normalized) moments corresponding to these projections are defined as:

$$J_n^{(\pm)}(\theta) := \frac{\int_{-\infty}^{\infty} s^n p^{(\pm)}(s, \theta) ds}{\int_{-\infty}^{\infty} p^{(\pm)}(s, \theta) ds} \tag{5}$$

3 DCCs and Calibration

3.1 Exploitable symmetries

Two symmetries underpin the proposed new set of DCCs. First, we consider a virtual detector on which the projections of points $\vec{q}$ are denoted by $\mathcal{P}(\vec{q})$, and the center of rotation as s_c, as illustrated in figure 2. This leads to the rotational symmetry

$$P(R_\theta(\vec{q})) = 2s_c - P(R_{\theta+\pi}(\vec{q})). \tag{6}$$

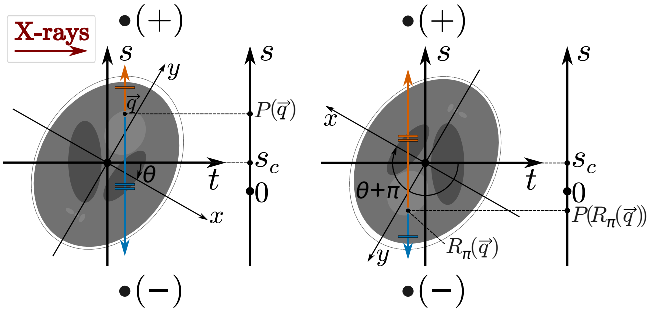

(a) Rotation θ (b) Rotation $\theta + \pi$

Figure 2 – Projection of the center of rotation s_c and point $\vec{q}$, denoted $P(\vec{q})$, on a virtual transmission detector with center $s = 0$ before (a) and after (b) a π-rotation.

Second, assuming that the detectors are placed symmetrically around the center of rotation — or can be approximated as such — there is a symmetry between the detectors for the outward transmission map, given by:

$$T_{\text{out}}^{(\pm)}(\vec{q}, \theta) = T_{\text{out}}^{(\mp)}(R_\pi(\vec{q}), \theta + \pi) \tag{7}$$

A rotation by π in the sample frame maps the $(\mp)$ detector onto the $(\pm)$ position, thereby swapping the outward transmission for all points $\vec{q}$ to the detectors.

3.2 DCCs and center-of-rotation determination

The difference in incoming transmission to a point $\vec{q}$ between π-separated pairs is defined as:

$$D(\vec{q}, \theta) := T_{\text{in}}(\vec{q}, \theta) - T_{\text{in}}(R_\pi(\vec{q}), \theta + \pi) \tag{8}$$

When rearranged to express $T_{\text{in}}(\vec{q},\theta)$, this relation can be substituted into equation 4, yielding two separate integrands. The integrand $D(\vec{q},\theta)f(\vec{q},\theta)T^{(\pm)}_{\text{out}}(\vec{q},\theta)$ may be neglected in two cases: (i) when attenuation of the incident beam is negligible, resulting in negligible values for $D(\vec{q},\theta)$; or (ii) when the integrand is approximately odd, as is the case, for example, for samples exhibiting radial symmetry. In such cases, the combination of equations 4, 6, and 7 leads to the following set of DCCs, which relate the projections observed by the two detectors:

$$p^{(\pm)}(s,\theta) = p^{(\mp)}(2s_c - s, \theta + \pi) \tag{9}$$

Consequently, substituting this result into equation 5 yields

$$J^{(\pm)}_n(\theta) = (-1)^n \sum_{k=0}^{n} \binom{n}{k} (-2s_c)^k J^{(\mp)}_{n-k}(\theta+\pi), \tag{10}$$

of which the $n = 1$ case yields a key calibration result, allowing for an explicit determination of the center of rotation:

$$s_c = \frac{1}{2}\left[J^{(+)}_1(\theta) + J^{(-)}_1(\theta+\pi)\right] \tag{11}$$

3.3 Sample Motion

Up to this point, sample motion has not been considered. To distinguish between *true* and *measured* quantities, measured values are denoted with an asterisk (*). The measured values differ from the true values due to projection-dependent sample motion, denoted by $\vec{m}(\theta)$, as illustrated in figure 3. Such motions shift the measured projections by $\Delta s(\theta)$, yielding a relation between the true and measured values of the first-order moment given by:

$$J^{(\pm)}_n(\theta) = \sum_{k=0}^{n} \binom{n}{k} [-\Delta s(\theta)]^k J^{*(\pm)}_{n-k}(\theta) \tag{12}$$

which follows from applying these shifts to the projections in equation 5. Substituting this result into equation 10 and solving for $n = 1$, gives

$$\begin{aligned} s_c = \frac{1}{2}\Big(&J^{*(+)}_1(\theta) + J^{*(-)}_1(\theta+\pi) \\ &- [\Delta s(\theta) + \Delta s(\theta+\pi)]\Big). \end{aligned} \tag{13}$$

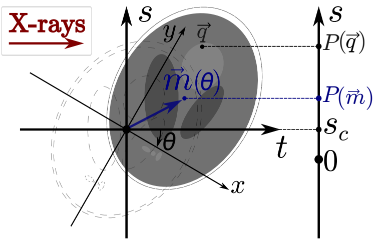

Figure 3 – At angle θ, the phantom's translation $\vec{m}(\theta)$ shifts all point projections $P(\vec{q})$ by $P(\vec{m}(\theta))$.

The sample motion is defined as a shift relative to some fixed point, whose projection offsets the entire fluorescence signal. Importantly, a constant component in these offsets is indistinguishable from a shift in the center of rotation. Therefore, the center of rotation and the motion must be defined jointly: the motion is expressed relative to a center of rotation such that it is evenly distributed around it. The center of rotation is then given by:

$$s_c = \frac{1}{4\pi}\int_0^{2\pi} \left(J^{*(+)}_1(\theta) + J^{*(-)}_1(\theta+\pi)\right) d\theta \tag{14}$$

and the sums of the pair-wise shifts by:

$$\Delta s(\theta) + \Delta s(\theta+\pi) = J^{*(+)}_1(\theta) + J^{*(-)}_1(\theta+\pi) - 2s_c \tag{15}$$

Thus, a constraint is obtained on the shifts $\Delta s(\theta)$ rather than a full description. However, by distributing these shifts evenly between both terms, they may be approximated as:

$$\Delta s(\theta) = \Delta s(\theta+\pi) \approx \frac{1}{2}[\Delta s(\theta) + \Delta s(\theta+\pi)] \tag{16}$$

Although the approximation does not hold in general, applying the correction consistently reduces the relative mean squared error (MSE) of the shifts, as shown in equation 17. Here, $\text{MSE}^{(s)}_{\text{i}}$ and $\text{MSE}^{(s)}_{\text{cor}}$ denote the pre- and post-correction errors, respectively, with the individual errors defined as the magnitudes of the residual shifts. Under pure noise and sufficient angular sampling, the correction yields a 50% reduction in MSE. Furthermore, if the shifts originate from random motion, the pairwise sums should fluctuate around zero without systematic trends. Deviations from this behavior indicate sample drift and offer a metric for its quantification.

$$\frac{\text{MSE}^{(s)}_{\text{i}} - \text{MSE}^{(s)}_{\text{cor}}}{\text{MSE}^{(s)}_{\text{i}}} = \frac{1}{2} + \frac{\int_0^{2\pi} \Delta s(\theta)\Delta s(\theta+\pi)d\theta}{2\int_0^{2\pi} \Delta s^2(\theta)d\theta} \tag{17}$$

4 Simulation

Simulations were conducted using the `corrct` package [9]. Projections from both detectors covered a full 2π rotation with 720 angular and 256 translational steps, sampled symmetrically about the center of rotation. The incident beam energy was set to 20 keV. Sample motion combined random noise with a structured component modeled as a sum of sine functions with random phases, frequencies, and amplitudes. The sample, based on the Shepp–Logan phantom, contains four material phases (Fig. 4). Incoming attenuation reached up to 22%, sufficient even for XTCT alignment.

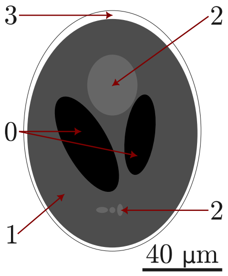

Phase	Density (g/cm^3)	Z	Mass fraction
0	0.0012	6 C	0.000124
		7 N	0.755267
		8 O	0.231781
		18 Ar	0.012827
1	2.8	6 C	0.120003
		8 O	0.479554
		20 Ca	0.400443
2	3.3	8 O	0.285299
		20 Ca	0.714701
3	5.3	8 O	0.300567
		26 Fe	0.699433

Figure 4 – Sample composition and phase definitions used in the phantom. Phases 0–3 correspond to air, calcium carbonate, calcium oxide, and ferric oxide, respectively.

5 Results

Results for center-of-rotation estimation in the motionless case are shown in figure 5. The individual moments $J_1^{(\pm)}(\theta)$ and their sum violate the Helgason–Ludwig conditions due to the unaccounted attenuation. The residual between the true and estimated center of rotation s_c is negligible when incoming attenuation is removed. The Fe signal exhibits greater deviation than Ca, attributed to its outer-shell distribution, which amplifies the difference in incoming transmission (equation 8) and reduces its negligibility. This deviation is independent of the element type or fluorescence energy and instead governed by spatial distribution.

Figure 6 shows motion estimates based on the Ca Kα signal. The estimates are π-periodic, as expected from equation 16. Although individual estimates may under- or over-shoot the ground truth, applying the correction reduces the MSE by 45% in this case. Performance depends strongly on the degree of π-periodicity: perfect periodicity yields perfect correction; odd periodicity yields none. Simulations with random motion confirm an average MSE reduction of 50%, consistent with equation 17. Adding Poisson noise has no impact, provided it does not significantly distort the moment.

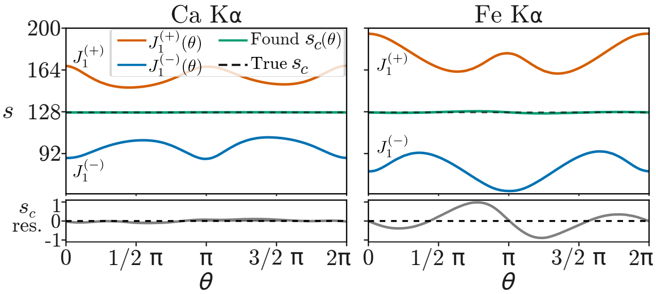

Figure 5 – Simulation results for the determination of the center of rotation s_c from the moments $J_1^{(\pm)}(\theta)$, as defined in equation 11, and comparison with the true center of rotation.

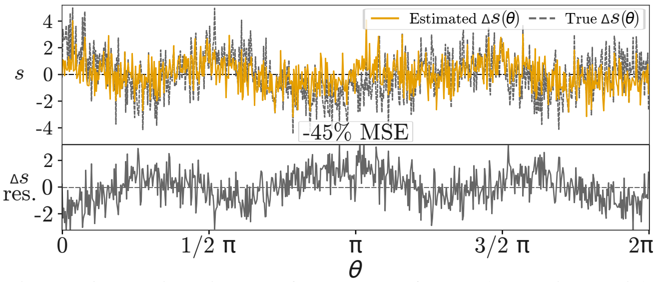

Figure 6 – Estimation performance of sample motion, with corresponding mean squared error (MSE) improvement.

6 Discussion

The accuracy of the center-of-rotation estimation using equation 11 is validated in figure 5. The residual between the estimated and true center of rotation is attributed to incident beam attenuation. This residual — which is largely symmetric over the domain — further reduces when averaged over multiple angular pairs, particularly in cases where incoming beam attenuation is already too low for reliable XTCT alignment.

In the presence of sample motion, deviations between individual pair-wise estimates and their mean reflect motion-induced shifts, assuming these dominate the effect of incoming attenuation. For purely random motion, this approach reduces the MSE by 50%, with variable improvement for other types of motion.

Notably, averaging the summed moments across the full domain — irrespective of the π-shifts — still yields the correct center of rotation, as shown by equation 14. Thus, standard Helgason–Ludwig transmission calibration remains valid for the summed signal, though it requires full-domain data and does not allow for estimation of shifts.

7 Conclusion

A novel set of XFCT-specific data consistency conditions (DCCs) is proposed and validated through simulation, accounting for self-absorption and operating under weak constraints on incoming beam attenuation. These DCCs enable determination of the center of rotation using a single pair of projections acquired from opposing detectors and separated by half a rotation. Additionally, the DCCs can be used to estimate and correct for sample motion, achieving up to a 50% reduction in mean squared error for random motion, with performance varying across different motion types.

References

[1] M. D. de Jonge et al. Spiral scanning x-ray fluorescence computed tomography. *Opt. Express*, 25(19):23424–23436, Sep 2017.

[2] J. Dengler. A multi-resolution approach to the 3d reconstruction from an electron microscope tilt series solving the alignment problem without gold particles. *Ultramicroscopy*, 30(3):337–348, 1989.

[3] T. Donath, F. Beckmann, and A. Schreyer. Automated determination of the center of rotation in tomography data. *Journal of the Optical Society of America A*, 23(5):1048–1057, 2006.

[4] C. A. S. Dunning and M. Bazalova-Carter. Sheet beam x-ray fluorescence computed tomography (xfct) imaging of gold nanoparticles. *Medical Physics*, 45(6):2572–2582, 2018.

[5] A. Kingston et al. Reliable automatic alignment of tomographic projection data by passive auto-focus. *Medical Physics*, 38(9):4934–4945, 2011.

[6] K. Radrich et al. Improving limited-projection-angle fluorescence molecular tomography using a co-registered x-ray computed tomography scan. *Journal of Biomedical Optics*, 17(12):126011, 2012.

[7] M. Guizar-Sicairos et al. Phase tomography from x-ray coherent diffractive imaging projections. *Opt. Express*, 19(22):21345–21357, Oct 2011.

[8] S. Helgason. *The Radon Transform*. Progress in Mathematics. Birkhäuser, Boston, MA, USA, 1999.

[9] N. Viganò and V. A. Solé. Physically corrected forward operators for induced emission tomography: a simulation study. *Measurement Science and Technology*, Advanced X-Ray Tomography:1–26, November 2017.